Neural network analysis of unstable temporal intensity peaks in continuous wave modulation instability

Mehdi Mabed, Lauri Salmela, Andrei Ermolaev, Christophe Finot, Goëry Genty, J.M. Dudley

Neural network analysis of unstable temporal intensity peaks in continuous wave modulation instability

Mehdi Mabed,[1] Lauri Salmela,[2] Andrei Ermolaev,[1]

Christophe Finot,[3] Goëry Genty,[2] and John M. Dudley[1,*]

[1] *Université de Franche-Comté, Institut FEMTO-ST, CNRS UMR 6174, 25000 Besançon, France*

[2] *Photonics Laboratory, Tampere University, FI-33104 Tampere, Finland*

[3] *Université de Bourgogne, Laboratoire Interdisciplinaire Carnot de Bourgogne, CNRS UMR 6303, 21078 Dijon, France*

(Dated: April 28, 2023)

Abstract

We report the application of a neural network to correlate spectral and temporal properties for modulation instability excited by a continuous wave field with random quantum noise. Using numerical simulations to generate large ensembles of chaotic modulation instability data, a trained neural network is shown to be able to correlate unstable intensity spectra and associated temporal intensity peaks with correlation coefficients exceeding $\rho = 0.90$ for dynamic ranges exceeding 40 dB. Such excellent correlation is obtained both in the initial evolving phase of modulation instability where spectra typically possess significant sideband structure, as well as in the stationary phase of the instability when distinct sideband structure is not apparent. For both cases, we also test the degree to which a neural network may be able to "forecast" temporal instability peaks based on analyzing spectral intensity at an earlier spatial reference position, but conclude that such forecasting is successful over only within a very localized distance range much less than the characteristic nonlinear length.

* Corresponding Author: john.dudley@univ-fcomte.fr

I. INTRODUCTION

The connection between solitons in optical fibers and the process of modulation instability has a long history, dating to the earliest days of nonlinear fiber optics and the farsighted work of Hasegawa and many other pioneers [1–4]. The study of modulation instability remains of great interest both in optics and in other fields, as theoretical and experimental advances continue to yield new insights into both the underlying physics, as well as into potential means of controlling the instability. A particular focus has been to understand potential analogies between localized regions of high intensity that emerge from modulation instability, and the properties of extreme rogue waves that appear more generally in nonlinear systems [5].

In parallel, there has also been much recent interest in applying machine learning techniques to gain insights into nonlinear fiber optics, including soliton physics [6]. Experimental studies, for example, have applied a range of optimization methods such as neural networks and genetic algorithms to identify optimal operating regimes of dissipative soliton modelocked fiber lasers [7], and to predict time series behaviour in chaotic lasers [8]. In addition, numerical studies have shown how neural networks can be used as emulators to replace direct integration of the non-linear Schrödinger equation (NLSE) that governs nonlinear propagation in optical fiber [9, 10], as well as to predict pulse profiles arising from NLSE propagation [11].

Another area of recent work in fiber systems has studied how neural networks can predict temporal instabilities (including rogue waves) based only on analyzing patterns in the corresponding frequency-domain intensity spectra. In fact, this has already been demonstrated for envelope modulation instability (MI) inducing the breakup of picosecond pulses [12], the emergence of frequency-shifted Raman solitons in supercontinuum generation [13], and the detection of random soliton peaks in a noise-like pulse fiber laser [14].

In a sense, the detection of temporal instability peaks based only on spectral intensity analysis should be difficult or even impossible, because the precise transformation between time and frequency domains requires knowledge of spectral phase [15]. However, the fact that this works so successfully reflects the powerful ability of a neural network to identify and correlate defining signatures of localized temporal structures, even within complex spectra associated with unstable propagation. From an experimental perspective, this is of particular interest in nonlinear fiber optics where the measurement of spectral instabilities in real-time is relatively straightforward when compared to equivalent real-time measurements in the time domain [16–18]. And while recent work has contributed to significant progress in understanding the physical origin of these high intensity

peaks, there remains clear interest in being able to potentially predict the emergence of extreme time-domain events based only on spectral measurements [19]

A potential shortcoming of these previous studies, however, is that they have all been performed for various generalized NLSE scenarios including higher order dispersive and nonlinear contributions [4]. There has not yet been a careful study to examine whether such correlations can also be identified by neural networks for the ideal case of chaotic MI induced by continuous wave (CW) excitation in the presence of noise. This paper fills this gap, and we show in particular how a neural network succeeds in spectral-temporal correlation in two regimes of CW MI: an early stage of propagation where the instability is still evolving and where intensity spectra show distinct sideband structure, as well as a later "stationary" regime observed at greater distances where spectral sideband structure is no longer apparent [20]. In addition, we consider the ability of a neural network to "forecast" the occurrence of MI temporal instabilities at a future stage of propagation based on analyzing spectral intensity at an earlier spatial reference position. We find, however, that such forecasting is successful within a very localized distance range of only a small fraction of a growth-decay evolution cycle.

II. METHODS

Our modelling is based on the nonlinear Schrödinger equation (NLSE) as written in dimensional form for fiber optics:

$$\mathrm{i}\frac{\partial A}{\partial z} - \frac{\beta_2}{2}\frac{\partial^2 A}{\partial T^2} + \gamma|A|^2 A = 0. \tag{1}$$

Here $A = A(z,T)$ is the field envelope evolving in space z and co-moving time T, with β_2 and γ the usual fiber group velocity dispersion and nonlinearity parameters respectively [4]. We consider MI developing from an incident CW field of power P_0, upon which is imposed a perturbation that seeds the instability. In the case of induced MI, this seed is typically a single-frequency harmonic modulation, but for spontaneous MI, we impose low amplitude random noise at the one photon per mode level [21]. In this case we see highly irregular evolution with random localized peaks in space and time that can be interpreted in terms of nonlinear breather structures [22–24].

Although we present results in dimensional units to make links with potential future experiments, since we only consider the ideal NLSE without any higher-order terms, the results below are completely applicable to any NLSE system. Indeed, we can transform into the dimensionless NLSE $\mathrm{i}\,u_\xi + 1/2\,u_{\tau\tau} + |u|^2\,u = 0$ with $u = A/P_0^{1/2}$, $\xi = z/L_{\mathrm{NL}}$, and $\tau = T/T_0$ with $T_0 = (|\beta_2|/\gamma\,P_0)^{1/2}$

and nonlinear length $L_{\rm NL} = (\gamma P_0)^{-1}$. We also note that the precise choice of noise source to seed the instability is unimportant, and similar results are obtained for a range of typical noise models [25]. We take realistic parameters of: $\beta_2 = -2.1 \times 10^{-26}\,{\rm s}^2\,{\rm m}^{-1}$, $\gamma = 1.1 \times 10^{-3}\,{\rm W}^{-1}\,{\rm m}^{-1}$ and $P_0 = 50\,{\rm W}$. For these parameters, the nonlinear length is $L_{\rm NL} \approx 18$ m.

The numerical method used is the standard split-step Fourier technique [4]. As a general rule for simulations of MI, the time window needs to be large enough so that we see a variety of localization scenarios and observe the full range of soliton on finite background solutions such as Akhmediev breathers and Peregrine solitons. We also require that the temporal resolution is sufficient to accurately resolve temporal peaks, and that the corresponding frequency window is such that we can clearly see the MI spectrum sitting on a background noise floor without truncation. For our fiber and power parameters, we expect the temporal structures to be separated (in a statistical average sense) by the reciprocal of the MI characteristic frequency $f_{\rm MI} = 1/2\pi(2\gamma P_0/|\beta_2|)^{1/2}$, suggesting temporal separation ∼2.7 ps. We therefore chose a time window of 110 ps such that we will typically observe ∼40 evolving structures, and with 2048 grid points, this is associated with a temporal resolution of 53.7 fs. Since typical high intensity peaks in the simulations were found to have ∼500 fs FWHM, this is sufficient for peak detection. For these parameters, the frequency span of 18.6 THz encompasses the full MI spectra, which was found to span ∼11 THz before reaching the background noise floor.

III. SIMULATION RESULTS

We model two regimes of MI. In the first, we consider the propagation of a noisy CW input over a total distance of 450 m. Figure 1 illustrates this regime of early stage propagation dynamics, where the evolution consists of an initial phase of instability development over ∼200 m, followed by ∼4 growth and decay cycles of the breather dynamics over the subsequent ∼250 m. Figs 1(a) and (b) plot typical spatio-spectral and spatio-temporal evolution respectively, with the results in (b) in particular showing the emergence from noise of a complex series of randomly evolving temporal peaks. Following the approach used for envelope MI in Ref. [12], we perform a large number (10000) of these simulations using different random noise seeds, saving the temporal and spectral intensity profiles at the end of the propagation segment. Figures 1(c) and 1(d) show results from 4 of these simulations where we see how the output spectral and temporal characteristics respectively vary significantly from shot to shot. Although it is not clear from visual inspection of the single shot spectra, the computed mean spectrum shows sideband structure reflecting the early stage of

evolution. The mean spectrum (over the 10000 simulations) is shown as the top curve in Fig. 1(c), and the inset to this figure shows an expanded view over a 20 nm span around the pump to highlight the sideband peaks. Our aim here is, based on each spectral intensity profile $S_k(\lambda)$, to attempt to predict the maximum intensity P_k anywhere within the temporal window. These points are shown as circles in Fig. 1(d).

The second regime of MI that we study considers propagation over a much greater distance of 550 km for the same initial conditions. In this case, we wish to analyse the spectral and temporal characteristics beyond the initial phase of propagation, in the stationary regime where the input evolves into fully-developed random (turbulent) MI with no apparent sideband structure [20]. To this end, we discard the evolution prior to a distance of 2.7 km ($\sim 150\, L_{\rm NL}$) and then from this point onwards, we extract 10000 spectral and temporal intensity profiles at 55 m intervals ($\sim 3\, L_{\rm NL}$) to form training and testing datasets. These results are shown in Fig. 2 and can be readily compared with the similar plots in Fig. 1. In Figs 2(a) and (b), however, we plot over a distance span of 300 m only when we have entered the stationary regime (this particular plot shows evolution far into the stationary regime starting at 55 km). The fact that we have entered into this particular stationary regime of dynamics (integrable turbulence) is apparent from the computed average spectrum shown in the inset of Fig. 2(c), which does not show any explicit sideband features [20, 24].

IV. NEURAL NETWORK RESULTS AND DISCUSSION

Figure 3(a) shows the neural network architecture that we use to correlate the spectral and temporal characteristics. In particular, we use a fully-connected feedforward neural network with two hidden layers to map an input spectrum spanning multiple wavelengths to a single scalar output corresponding to the maximum intensity of the associated temporal profile. The spectral sampling points and dynamic range influence the network performance, and to pre-process the input data in a way similar to experimental measurements, we convolve each spectrum with a 1 nm spectral gaussian response, and downsample to a specified number of sampling points. We also transform to a logarithmic (dB) scale and truncate to a specified dynamic range with the addition of a random numerical noise floor.

The network design has been previously presented in detail in Ref. [17] but for completeness, we give a brief summary here. The input is a spectral intensity vector $X^{(0)} = \left[x_1^{(0)}, x_2^{(0)}, \ldots, x_{N_0}^{(0)}\right]$ of length $N_0 = 150$, whilst the network output is a single scalar y equal to the maximum intensity of the corresponding temporal profile. The input vector is transformed using the standard approach

for a feedforward network where the value of a generic neuron in a given hidden layer $h_i^{(k)}$ (i^{th} neuron in layer k) is constructed from a parameterized linear transformation of the neurons in the preceding layer $h^{(k-1)}$, followed by a nonlinear transformation ("activation function"). Specifically, for weight and bias parameters w and b respectively, and for hyperbolic tangent activation function, we can write:

$$h_i^{(1)} = \tanh\left(\sum_{j=1}^{N_0} w_{ij}^{(1)} x_j^{(0)} + b_i^{(1)}\right)$$

This procedure then repeats to compute the values of the second hidden layer $h^{(2)}$ and once again to compute the output y which is the prediction of the network. A defined cost function (quadratic or mean-squared error) measures the error between the true value that the network should have predicted (the target) and its actual prediction; and a standard gradient descent training method is used to update the weights and biases in order to minimize the error. This procedure was implemented here using a conjugate gradient backpropagation algorithm with Fletcher-Reeves updates. We used 300 passes through the training dataset (epochs) for all results in this paper. Additional details about the methods used can be found in e.g. [26]. Out of the 10000 simulations, 7500 were used in training and 2500 in testing. As discussed further below, Fig. 3(b) shows results examining the network performance for different numbers of neurons in each hidden layer.

Figure 4 shows results of network training and testing for the early stage propagation regime (Fig. 1). Specifically, we consider an architecture of 150 and 10 nodes in the two hidden layers, input data consisting of 150 wavelength points over a 150 nm span, and simulation resolution-limited dynamic range (i.e. no truncation) of ∼100 dB. Note that the wavelength sampling was found to play a minor role and essentially identical results are obtained using input data downsampled to 50 points. The testing procedure quantifies how the network estimates the maximum intensity in the temporal MI field from a given spectrum, comparing the predicted value with the known (ground-truth) value in a correlation plot. The results in Fig. 4(a) show excellent results with clear grouping around the expected $x = y$ linear relationship (white dashed line), and a very high correlation coefficient of $\rho = 0.99$.

Figure 4(b) shows testing results for a significantly truncated dynamic range of 40 dB (keeping the wavelength span and number of sampling points the same) where we see that good correlation coefficient with ~ 0.92 is still attainable. To study this in more detail, Fig. 4(c) plots the dependence of the test correlation for truncation over the range 20-100 dB, suggesting that 40 dB is a practical limit for input data to the network. This dependence on dynamic range is not surprising since the detection of high intensity peaks in the time domain will necessarily be correlated physically

with the larger bandwidths associated with structure in the spectral wings, and it is exactly this structure that is removed with truncation.

Figure 5 shows similar results, but for the case of simulation data obtained in the stationary regime of MI propagation (Fig. 2). As is clear from comparison of the results in Figs 4 and 5, the correlation plots and the dependence on dynamic range are essentially identical. This suggests that any potential spectral sideband structure near the pump plays negligible role in driving the correlation, and this is consistent with the remark above concerning the fact that the highest intensity peaks in the time domain will necessarily be correlated with the extension in the spectral wings. These results are important in confirming the network's performance given that training uses only intensity data without any phase information.

We also note that we tested the neural network performance with data sets obtained from simulations with different time windows. In particular, we used a doubled time span of 220 ps with 4096 points (which increases the number of temporal structures in the computation window but with the same temporal resolution and same frequency span) and we also used a halved time span of 55 ps with 2048 points (which reduces the number of temporal structures observed, but which improves the temporal resolution and increases the frequency span). In both cases we obtained results that were essentially indistinguishable from those shown above.

Note that we also used simulation data in the stationary regime with maximum dynamic range to test the performance of the network for different architectures with different numbers of neurons in the first and second hidden layers between 10-310 and 10-110 respectively. These results are shown in the grid in Fig. 3(b) and we can clearly see that high correlation is obtained for a broad range of architectures. The global maximum within this range was observed for 150 and 10 neurons in the two hidden layers, which was the choice of design used for all results in this paper. Note that because the optimization of coefficients in a neural network begins from randomly chosen initial values and can vary between training runs even using identical training data, we performed 5 training runs for each network architecture; the results plotted in the figure are the mean values.

It is interesting to see from the grid search results in Fig. 3(b) that the accuracy of the network appears to degrade as the number of neurons in the second hidden layer increases. We attribute this to overfitting that results from the increased learning capacity of the network with a larger number of neurons [26]. Increased learning capacity in this context can lead to a generalisation error, i.e. even though the network can perform extremely well on the training data, the generalisation of the network is poor and degraded performance is observed when the network is applied on new data. In a general context, the training of a neural network is well-known to be highly dependent on

the architecture and parameters of the network (e.g. the number and size of layers), the training process (e.g. conjugate gradient or steepest descent), as well as on the data that the network is trained with and the particular features in the data that one is attempting to correlate. Although some rules of thumb have been developed for some situations [27], it is generally accepted that there are no rigorous criteria that apply in all circumstances [26]. Indeed in the general case, it is only through systematic grid searches such as that which we have performed here that one can reliably identify a parameter regime that yields good results.

Finally, we also studied if a network is able to "predict" the emergence of MI peaks based on analyzing spectra at an earlier stage of propagation from that at which the temporal intensity peak was extracted and used in training. Figures 6(a) and 6(b) show these results for both early stage and stationary propagation regimes respectively. For both cases we plot the obtained (test) correlation coefficient as a function of $\Delta z/L_{\mathrm{NL}}$, the distance between the spectra used as input to the network and the target temporal profile, expressed as a percentage of the nonlinear length. Although the correlation rapidly falls with distance, we are able to establish limits on the useful ($\rho > 0.8$) predictive power of the network as associated with distance $\Delta z \approx 0.1 L_{\mathrm{NL}}$. Although from a predictive point of view, these results suggest that there is rapid decorrelation between temporal and spectral properties with propagation distance, establishing this limit quantitatively is nonetheless useful.

V. CONCLUSIONS

The results shown here have shown that simple feedforward neural networks can accurately correlate spectral and temporal intensity characteristics in continuous wave modulation instability described by the ideal nonlinear Schrödinger equation. These results complement previous work studying similar correlations under conditions of pulsed excitation and in the presence of higher-order effects. We have also explicitly shown that such spectral-temporal correlation is successful both in the initial evolving phase of modulation instability where spectra typically possess sideband structure, as well as the stationary phase of the instability when sideband structure is not apparent.

For both cases, we have also tested whether a neural network may be able to forecast the properties of temporal instability peaks based on analyzing spectra at an earlier spatial reference position, but our results show that this is possible only over a very small fraction of a nonlinear length. In fact, from a physical perspective, the growth and decay of a particular temporal structure typically occurs over a distance scale of several L_{NL}, and so what these results suggest is that any

correlation is limited within the extent of a small fraction of the growth and decay lifetime of each emergent peak. In other words, this highlights the independence and incoherence between sequential emerging peaks that develop within the modulation instability field.

Overall, the results presented here provide a further example of the utility of neural networks in being able to analyse complex dynamics in nonlinear Schrödinger equation systems. Further areas of work would be expected to consider more general scenarios including modulation instability in the presence of convective effects (third order dispersion) and for the case of excitation with a partially coherent pump [24, 28, 29].

VI. ADDITIONAL INFORMATION

DATA AND CODE AVAILABILITY

Data are available from the corresponding author upon reasonable request. The results in the manuscript were obtained using standard techniques for solving the nonlinear Schrödinger equation [4] to generate the MI data, as well as neural network code suites within the MATLAB Global Optimization toolbox.

ACKNOWLEDGEMENTS

M.M. and J.M.D.acknowledge support from the French Investissements d'Avenir programme, project ISITE-BFC (ANR-15-IDEX-0003) and project EUR (ANR-17-EURE-0002). G.G. and L.S. acknowledge support from the Academy of Finland (Grants 318082, 333949, Flagship PREIN 320165). J.M.D. and C. F. also acknowledge project ANR-20-CE30-0004 and the CNRS programme MITI (Mission Initiatives Transverses et Interdisciplinaires Evenements Rares).

AUTHOR CONTRIBUTIONS STATEMENT

M.M. and J.M.D. developed and ran the code for modelling fiber propagation and for neural network training. Data analysis and interpretation of the results was performed by all authors. J.M.D. also provided overall project supervision. All authors contributed to writing of the manuscript.

COMPETING INTERESTS

The authors declare no competing interests.

REFERENCES

[1] Hasegawa, A. & Tappert, F. Transmission of stationary nonlinear optical pulses in dispersive dielectric fibers. i. anomalous dispersion. *Applied Physics Letters* **23**, 142–144 (1973).

[2] Hasegawa, A. & Brinkman, W. Tunable coherent ir and fir sources utilizing modulational instability. *IEEE Journal of Quantum Electronics* **16**, 694–697 (1980).

[3] Zakharov, V. & Ostrovsky, L. Modulation instability: The beginning. *Physica D: Nonlinear Phenomena* **238**, 540–548 (2009).

[4] Agrawal, G. P. *Nonlinear Fiber Optics*. Optics and Photonics (Academic Press, Boston, 2019).

[5] Dudley, J. M., Genty, G., Mussot, A., Chabchoub, A. & Dias, F. Rogue waves and analogies in optics and oceanography. *Nature Reviews Physics* **1**, 675–689 (2019).

[6] Genty, G. *et al.* Machine learning and applications in ultrafast photonics. *Nature Photonics* **15**, 91–101 (2020).

[7] Meng, F. & Dudley, J. M. Toward a self-driving ultrafast fiber laser. *Light: Science & Applications* **9**, 26 (2020).

[8] Nonaka, M., Agüero, M. & Kovalsky, M. Machine learning algorithms predict experimental output of chaotic lasers. *Optics Letters* **48**, 1060–1063 (2023).

[9] Salmela, L. *et al.* Predicting ultrafast nonlinear dynamics in fibre optics with a recurrent neural network. *Nature Machine Intelligence* **3**, 344–354 (2021).

[10] Salmela, L. *et al.* Feed-forward neural network as nonlinear dynamics integrator for supercontinuum generation. *Optics Letters* **47**, 802–805 (2022).

[11] Boscolo, S. & Finot, C. Artificial neural networks for nonlinear pulse shaping in optical fibers. *Optics & Laser Technology* **131**, 106439 (2020).

[12] Närhi, M. *et al.* Machine learning analysis of extreme events in optical fibre modulation instability. *Nature Communications* **9**, 4923 (2018).

[13] Salmela, L., Lapre, C., Dudley, J. M. & Genty, G. Machine learning analysis of rogue solitons in supercontinuum generation. *Scientific Reports* **10**, 9596 (2020).

[14] Mabed, M. *et al.* Machine learning analysis of instabilities in noise-like pulse lasers. *Optics Express* **30**, 15060–15072 (2022).

[15] Trebino, R. *Frequency-Resolved Optical Gating: The Measurement of Ultrashort Laser Pulses* (Springer, 2000).

[16] Goda, K. & Jalali, B. Dispersive fourier transformation for fast continuous single-shot measurements. *Nature Photonics* **7**, 102–112 (2013).

[17] Närhi, M. *et al.* Real-time measurements of spontaneous breathers and rogue wave events in optical fibre modulation instability. *Nature Communications* **7**, 13675 (2016).

[18] Godin, T. *et al.* Recent advances on time-stretch dispersive fourier transform and its applications. *Advances in Physics: X* **7**, 2067487 (2022).

[19] Akhmediev, N., Ankiewicz, A., Soto-Crespo, J. M. & Dudley, J. M. Rogue wave early warning through spectral measurements? *Physics Letters A* **375**, 541–544 (2011).

[20] Gelash, A. *et al.* Bound State Soliton Gas Dynamics Underlying the Spontaneous Modulational Instability. *Physical Review Letters* **123**, 234102 (2019).

[21] Dudley, J. M., Genty, G. & Coen, S. Supercontinuum generation in photonic crystal fiber. *Reviews of Modern Physics* **78**, 1135–1184 (2006).

[22] Akhmediev, N. & Ankiewicz, A. *Solitons. Non-linear pulses and beams.* (Springer, 1997).

[23] Toenger, S. *et al.* Emergent rogue wave structures and statistics in spontaneous modulation instability. *Scientific Reports* **5**, 10380 (2015).

[24] Copie, F., Randoux, S. & Suret, P. The physics of the one-dimensional nonlinear schrödinger equation in fiber optics: Rogue waves, modulation instability and self-focusing phenomena. *Reviews in Physics* **5**, 100037 (2020).

[25] Frosz, M. H. Validation of input-noise model for simulations of supercontinuum generation and rogue waves. *Optics Express* **18**, 14778–14787 (2010).

[26] Goodfellow, I., Bengio, Y., Courville, A. & Bach, F. *Deep Learning* (MIT Press, 2017).

[27] Stathakis, D. How many hidden layers and nodes? *International Journal of Remote Sensing* **30**, 2133–2147 (2009).

[28] Sauter, A., Pitois, S., Millot, G. & Picozzi, A. Incoherent modulation instability in instantaneous nonlinear kerr media. *Opt. Lett.* **30**, 2143–2145 (2005).

[29] Mussot, A. *et al.* Optical fiber systems are convectively unstable. *Phys. Rev. Lett.* **101**, 113904 (2008).

FIGURES

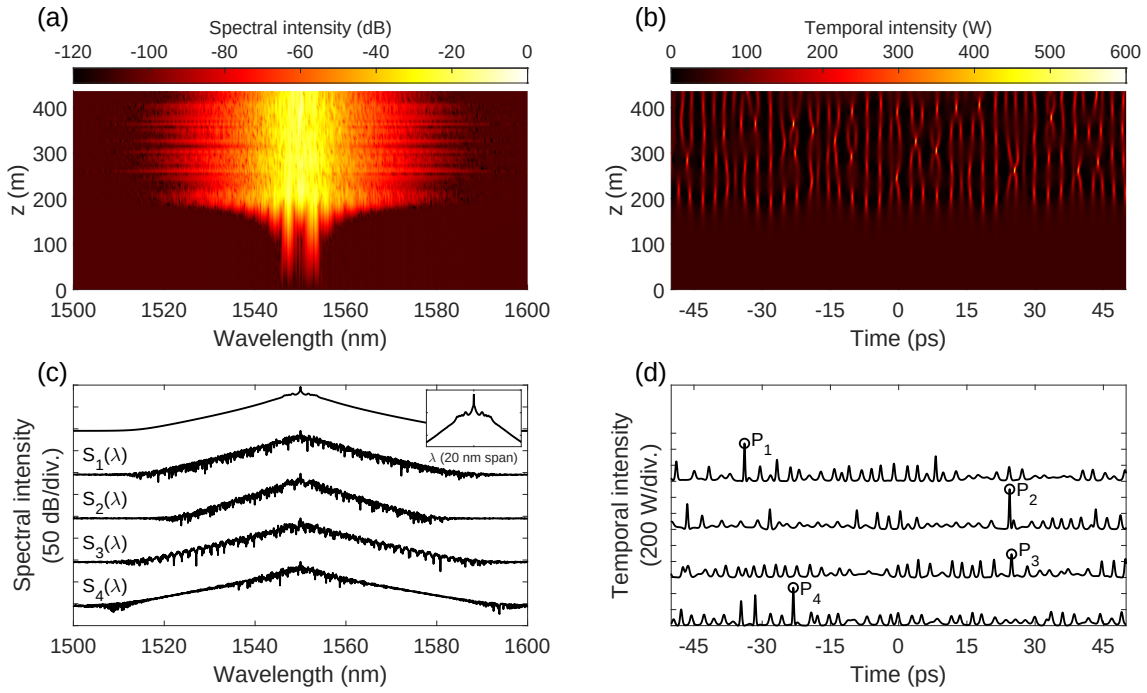

FIG. 1. Simulated MI dynamics from CW excitation in the early stage propagation regime. (a) Spectral and (b) temporal evolution over 450 m for one simulation. (c) Spectral and (d) temporal intensity (at the fiber output) from 4 different simulations. (c) also shows the computed mean (top) and a zoom in the neighbourhood of the pump (inset). The inset is plotted over a 20 nm span and over 50 dB dynamic range. In (d) the peak P_k in each case is shown by a circle, and this is the parameter that we are aim to predict from the corresponding single-shot spectra. For the purpose of clearly displaying multiple single-shot simulation results, an artificial vertical offset between different profiles is added in (c) and (d).

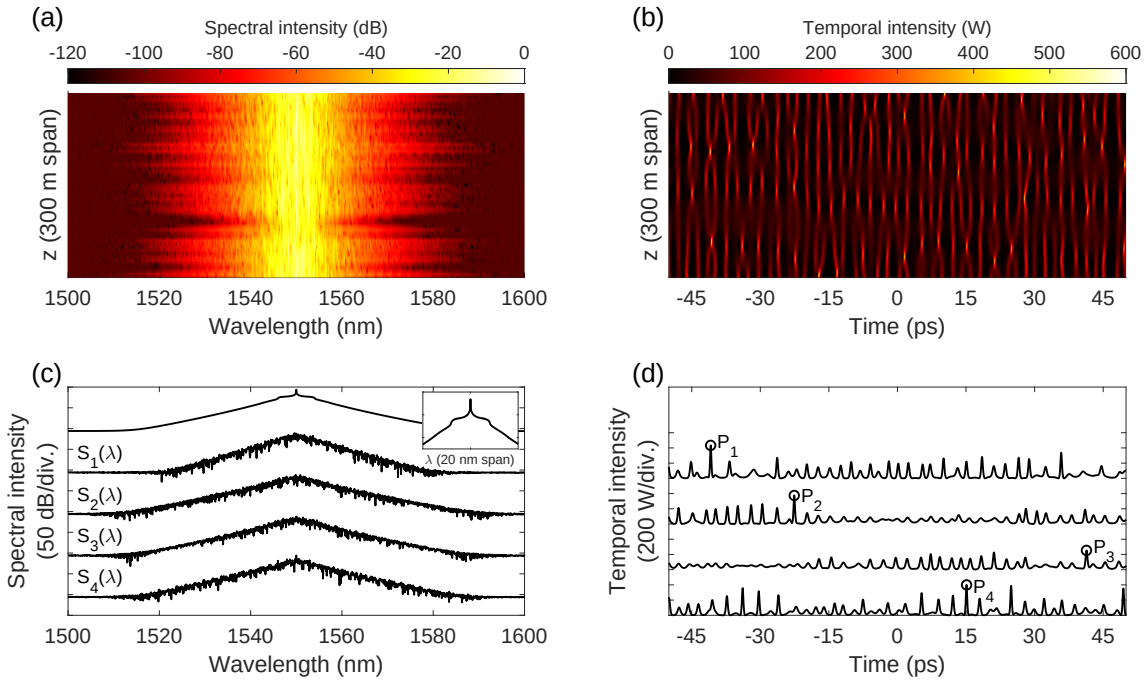

FIG. 2. Simulated MI dynamics from CW excitation in the stationary propagation regime. (a) Spectral and (b) temporal evolution over a distance of 300 m, beginning at 55 km when we are well in the stationary regime. (c) Spectral and (d) temporal intensity profiles extracted at 55 m intervals. (c) also shows the computed mean (top) and a zoom in the neighbourhood of the pump (inset). The inset is plotted over a 20 nm span and over 50 dB dynamic range. In (d) the peak temporal intensity in each case is shown by a circle, and this is the parameter that we aim to predict from the corresponding single-shot spectra. For the purpose of clearly displaying multiple single-shot simulation results, an artificial vertical offset between different profiles is added in (c) and (d).

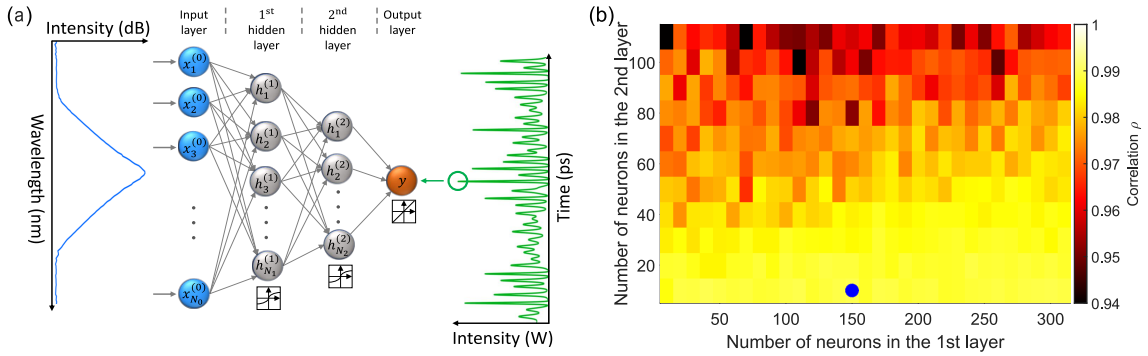

FIG. 3. (a) Schematic of the feedforward network design used in our study (150 points at the input, 150 neurons in the first hidden layer, 10 neurons in the second hidden layer, and one output). (b) Map of test correlation coefficient obtained as a function of the neural network architecture (number of neurons in each hidden layer) for the stationary MI regime. The blue circle indicates the particular architecture chosen for the study.

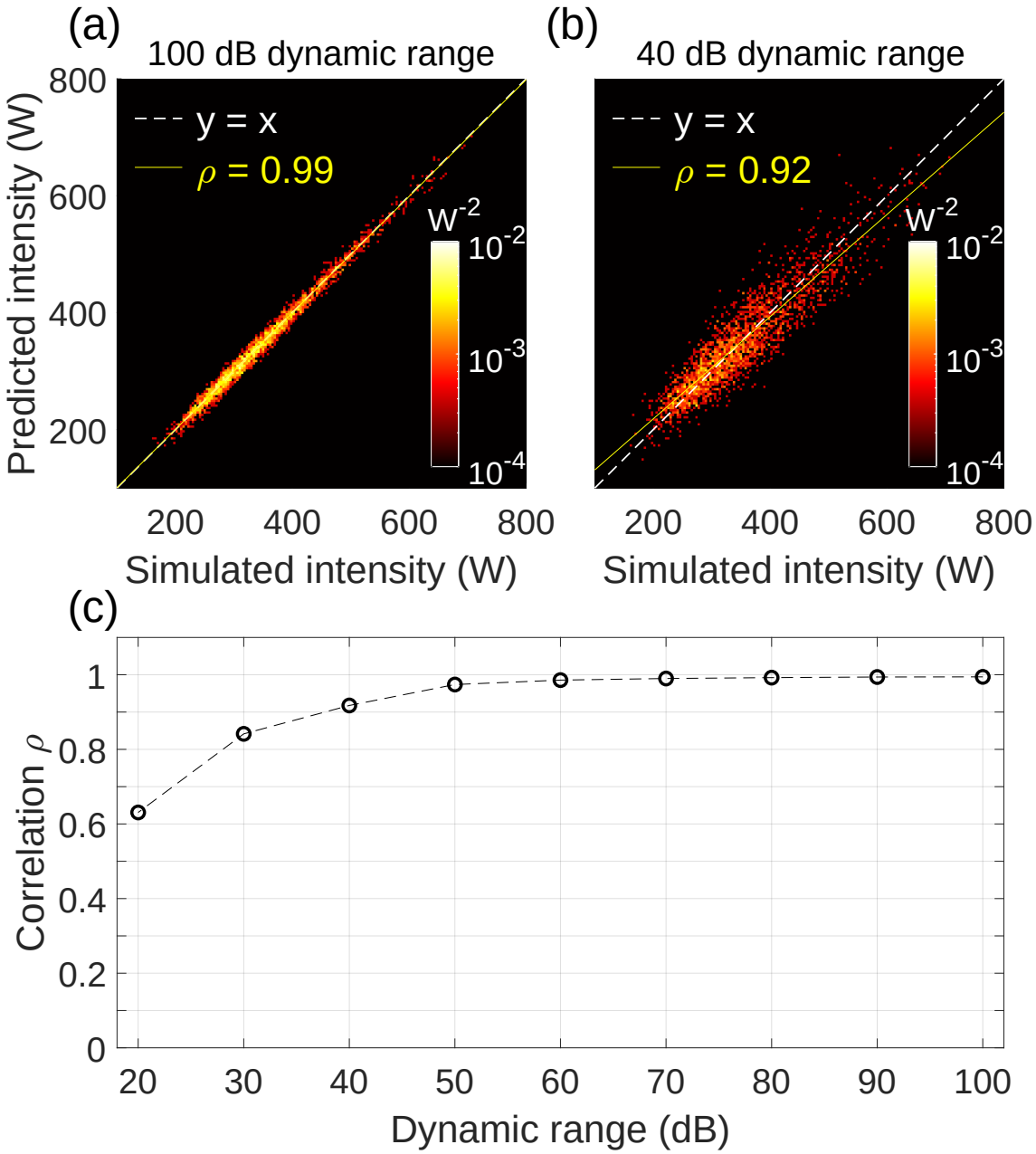

FIG. 4. Neural network performance for the early stage propagation regime, quantifying neural network prediction of temporal MI peaks based only on input spectral data. These results were based on an ensemble of 2500 simulations not used in the training phase. We compare the predicted peak power of the highest intensity temporal peak with the known result from simulations for input spectra: (a) with the full 100 dB dynamic range of simulations, (b) truncated to a dynamic range of 40 dB. (c) Plots the achieved correlation coefficient after testing as a function of dynamic range over 20–100 dB.

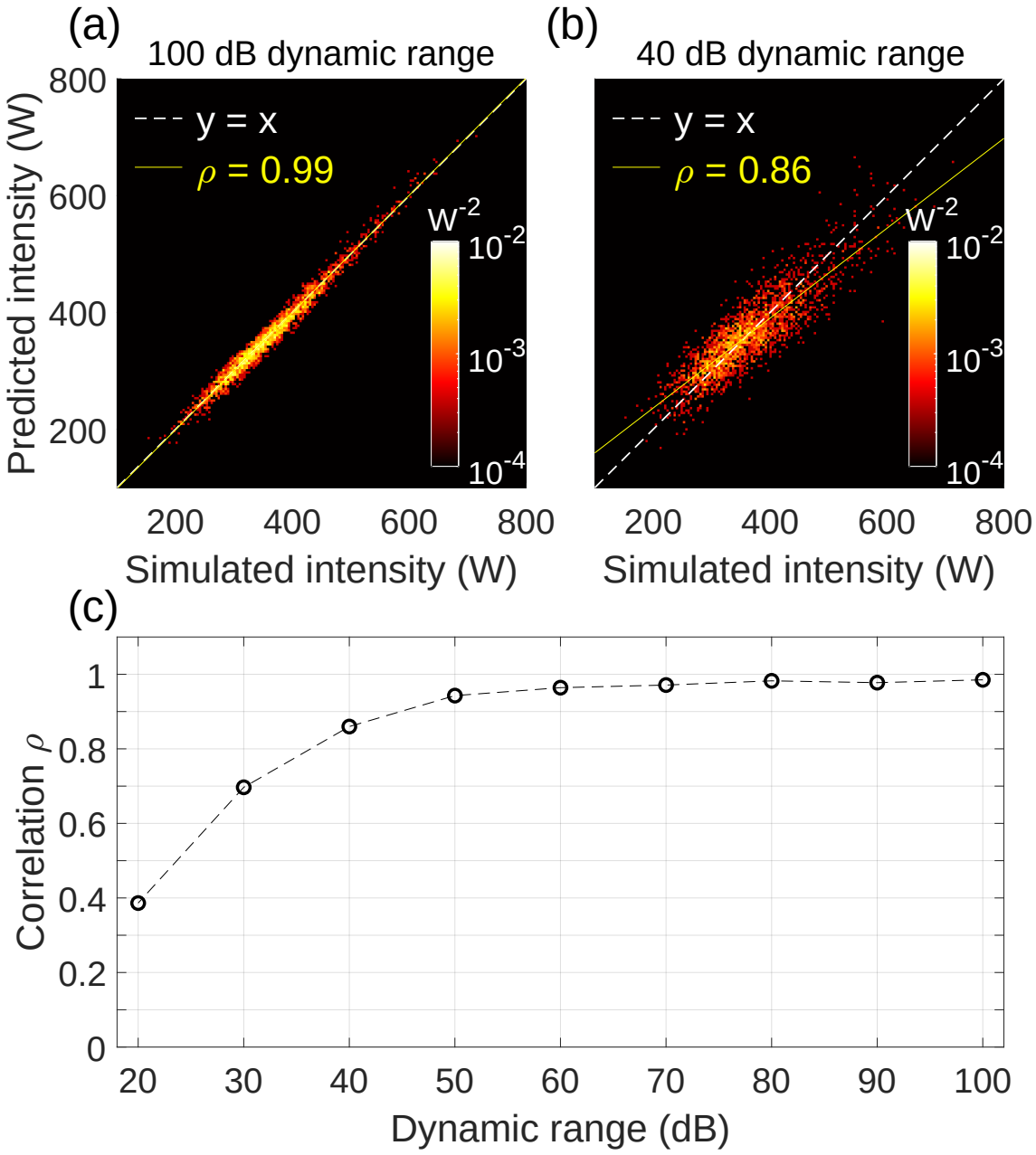

FIG. 5. Neural network performance for the stationary propagation regime, quantifying neural network prediction of temporal MI peaks based only on input spectral data. These results were based on an ensemble of 2500 simulations not used in the training phase. We compare the predicted peak power of the highest intensity temporal peak with the known result from simulations for input spectra: (a) with the full 100 dB dynamic range of simulations, (b) truncated to a dynamic range of 40 dB. (c) Plots the achieved correlation coefficient after testing as a function of dynamic range over 20–100 dB.

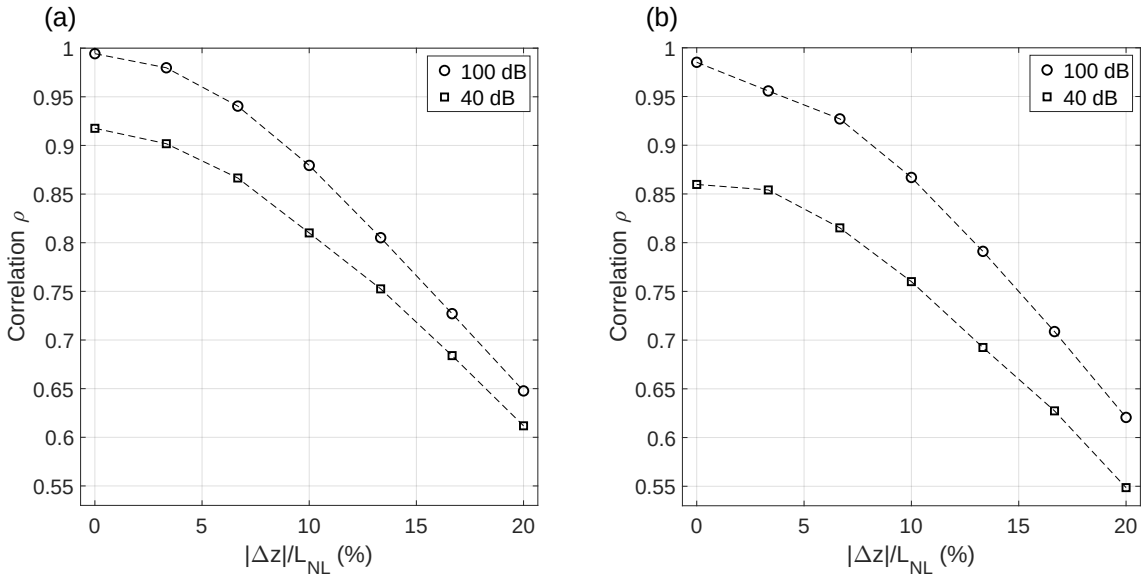

FIG. 6. Test correlation coefficient for (a) early stage and (b) stationary propagation regimes as a function of $\Delta z/L_{\mathrm{NL}}$, the distance between the target temporal profile used in training and that used in this predictive test. The distances are expressed as a percentage of the nonlinear length. Results are plotted for two dynamic ranges as shown.